

Research paper

Exceptional photocatalytic activities for CO₂ conversion on Al–O bridged g-C₃N₄/α-Fe₂O₃ z-scheme nanocomposites and mechanism insight with isotopesZ



Jinshuang Wang, Chuanli Qin*, Hongjian Wang, Mingna Chu, Amir Zada, Xuliang Zhang, Jiadong Li, Fazal Raziq, Yang Qu, Liqiang Jing*

Key Laboratory of Functional Inorganic Materials Chemistry (Heilongjiang University), Ministry of Education, School of Chemistry and Materials Science, International Joint Research Center for Catalytic Technology, Harbin 150080, PR China

ARTICLE INFO

Keywords:
G-C₃N₄/α-Fe₂O₃ nanocomposite
Al–O bridge
Z-scheme mechanism
CO₂ conversion
Photocatalysis

ABSTRACT

It's highly desired to design and fabricate effective Z-scheme photocatalysts by promoting the charge transfer and separation. Herein, we firstly fabricated the ratio-optimized g-C₃N₄/α-Fe₂O₃ nanocomposites by adjusting the mass ratio between two components through a simple wet-chemical process. The resulting nanocomposites display much high photocatalytic activities for CO₂ conversion and phenol degradation compared to bare α-Fe₂O₃ and g-C₃N₄. Noteworthily, the photocatalytic activities are further improved by constructing Al–O bridges, by 4-time enhancement compared to those of α-Fe₂O₃. Based on the steady-state surface photovoltage spectra, transient-state surface photovoltage responses, photoelectrochemical I-t curves and the evaluation of produced ·OH amounts, the exceptional photoactivities of Al–O bridged g-C₃N₄/α-Fe₂O₃ nanocomposites are attributed to the significantly promoted charge transfer and separation by constructing the g-C₃N₄/α-Fe₂O₃ heterojunctions and the Al–O bridges. Moreover, the charge transfer and separation of this photocatalyst have been confirmed to obey the Z-scheme mechanism, as supported by the single-wavelength photocurrent action spectra and single-wavelength photoactivities for CO₂ conversion. Furthermore, the mechanism of the photocatalytic CO₂ conversion has been elaborately elucidated through the electrochemical reduction and the photocatalytic experiments especially with isotope ¹³CO₂ and D₂O, that the produced H atoms as intermediate radicals would dominantly induce the conversion of CO₂ to CO and CH₄.

1. Introduction

The excessively exhausted gases, like carbon dioxide (CO₂) as a main greenhouse gas, are recognized to be the culprit causing the global climate change [1]. It's estimated that a double increase of the atmospheric CO₂ concentration would cause a global temperature rise of approximately 3 °C (with a probable uncertainty range of 2–4.5 °C) [2]. The accompanying freak weather, land desertification, sea level rise and widespread amphibian extinctions from epidemic disease hence would occur in high frequency [3–5]. Therefore, it's urgent to cut down the atmospheric CO₂ concentration effectively. In addition, as a vital link of carbon cycle, CO₂ could be utilized as the raw material to produce valuable chemicals [6,7]. Hence, it's rather meaningful to develop an efficient technique to convert CO₂ for reducing the greenhouse effect and producing value-added chemicals [8]. Moreover, organic contaminant pollution is another environmental threat for water body. As a typical contaminant among various organic ones, phenol greatly harms

the environment due to its high toxicity and bio-recalcitrant nature [9,10]. Therefore, it is highly desired to develop novel, green and sustainable technologies for CO₂ conversion and phenol degradation for the purpose of long-term development of human society.

Noteworthily, the photocatalytic technology is promising to solve the above-mentioned environmental problems, compared with the conventional technologies [11]. Photocatalysis is a clean and environmentally friendly process by utilizing solar energy, in which a semiconductor as the photocatalyst is excited by light to generate electrons and holes so as to induce reduction and oxidation reactions, respectively [12]. The chemical nature of the photocatalyst primarily leads to the efficiency of the photocatalytic process. Among distinct types of photocatalysts, single-metal oxides such as TiO₂, ZnO, SnO₂, WO₃, Bi₂O₃ and Fe₂O₃ are mostly investigated [13–18]. Since the visible light occupies 44% of the actual solar light spectrum, narrow-bandgap oxides capable of absorbing more visible light hence become the predominant choice. The narrow-bandgap α-Fe₂O₃ (band gap

* Corresponding authors.

E-mail addresses: qinchuanli@hlju.edu.cn (C. Qin), jinglq@hlju.edu.cn (L. Jing).

energy equals 2.0–2.2 eV) is widely applied due to its low cost, high stability, non-toxicity and magnetism [19,20]. However, its photocatalytic activities are limited mainly by the weak charge separation [21]. For this, several methods have been developed, such as nanosstructured construction, heterojunctional fabrication and elemental doping [22,23].

Additionally, from the thermodynamics view of point, the low conduction band (CB) bottom level of $\alpha\text{-Fe}_2\text{O}_3$ corresponds to the photo-induced electrons with the low energy, which is hardly capable of inducing reduction reactions with adsorbed H_2O , CO_2 and O_2 . This is mainly responsible for its weak photocatalytic performance [24]. Unfortunately, the above-mentioned factor limiting the activity of $\alpha\text{-Fe}_2\text{O}_3$ is often neglected. To overcome the shortfall, targeted modification strategies have been successfully developed to enhance the photocatalytic activities. For example, noble metals as co-catalysts could be integrated with $\alpha\text{-Fe}_2\text{O}_3$ [25]. In this case, the photo-induced electrons immigrate to the metals serving as the catalytic sites. However, the high cost of noble metals limits the practical application. While another feasible strategy is to couple $\alpha\text{-Fe}_2\text{O}_3$ with wide-bandgap semiconductors, like TiO_2 , which could afford a high-level-energy platform to accept the photo-induced electrons from $\alpha\text{-Fe}_2\text{O}_3$, hence improving the photocatalytic activities [26]. However, it is an uncommon electron transfer process from $\alpha\text{-Fe}_2\text{O}_3$ to the wide bandgap oxides with a high-level conduction band, leading to the low efficiency. Therefore, it is much meaningful to develop a novel and effective strategy to significantly facilitate the charge separation of $\alpha\text{-Fe}_2\text{O}_3$ in order to obtain enhanced photocatalytic performance.

Recently, a Z-scheme heterojunction strategy for $\alpha\text{-Fe}_2\text{O}_3$ by simulating the natural photosynthesis to couple another narrow bandgap semiconductor has been well investigated [27–29]. For the Z-scheme photocatalyst, $\alpha\text{-Fe}_2\text{O}_3$ and the coupled semiconductor would be simultaneously excited under light irradiation. Reasonably, the photo-induced electrons of $\alpha\text{-Fe}_2\text{O}_3$ would transfer to the coupled semiconductor for recombining holes. Thus, residual holes in $\alpha\text{-Fe}_2\text{O}_3$ exhibit strong oxidizing capacity, while the photo-induced electrons of the coupled semiconductor possess strong reducing capacity. Consequently, the designed Z-scheme $\alpha\text{-Fe}_2\text{O}_3$ -based photocatalyst would exhibit the much high photocatalytic activity [30]. To successfully construct a Z-scheme photocatalyst, the CB bottom level of the coupled semiconductor should be emphatically considered referring to the energy band structure of $\alpha\text{-Fe}_2\text{O}_3$. Graphitic carbon nitride ($\text{g-C}_3\text{N}_4$) is a metal-free, robust, low-cost and visible light responsible polymeric semiconductor, which has been proven to be the appropriate candidate since its CB and valence band (VB) are positioned at –1.14 and 1.57 eV, respectively [31–33]. The $\text{g-C}_3\text{N}_4/\alpha\text{-Fe}_2\text{O}_3$ nanocomposites have been reported to demonstrate much high activity compared with those of bare $\alpha\text{-Fe}_2\text{O}_3$ and $\text{g-C}_3\text{N}_4$ [34–36]. Nevertheless, the specific electron transfer mechanism for this Z-scheme photocatalyst is still ambiguous to date and needed to verify with solid evidences.

Although the Z-scheme design has shown obvious advantages, the lattice mismatch of different constituents would hinder the charge transfer and separation, which is overlooked in most cases [37]. As a targeted approach, to build electron shuttling bridges between the semiconductors would address this mismatching problem. Generally, noble metals like Pd and Au as effective conductors could shuttle electrons for Z-scheme photocatalyst. However, it is unsatisfactory due to the high cost [38,39]. Thus, the cheaper electron bridges are needed to explore. Inspired by our previous works, the functional groups like $-\text{P-OH}$ and $-\text{Si-OH}$ could effectively connect constituents of the heterojunctional photocatalyst, such as ZnO/BiVO_4 , $\text{TiO}_2/\text{Fe}_2\text{O}_3$ and $\text{TiO}_2/\text{g-C}_3\text{N}_4$, leading to the promoted charge transfer and separation and hence to enhanced photoactivities [40,41]. This indicates that the inorganic polyhydroxy groups like $-\text{Al-OH}$ possibly serve as feasible electron bridges. Besides, the electron transfer mechanism for the Z-scheme photocatalyst with polyhydroxy group bridges has seldom been investigated. Therefore, it is urged to be raveled.

Under the light irradiation, the photo-induced electrons and holes of designed heterojunctional photocatalyst would induce CO_2 conversion and pollutant degradation with complex photophysical and photochemical processes [42,43]. It is widely accepted that the produced $\cdot\text{OH}$ by oxidation between photo-induced holes and H_2O is regarded as the primary active species. The $\cdot\text{OH}$ radicals would further evolve O_2 in CO_2 conversion and directly attack organics to induce the pollutant degradation, respectively [44,45]. Therefore, it's reasonable and feasible to investigate the photo-induced charge separation by measuring the amount of produced $\cdot\text{OH}$. Currently, most works mainly focus on the improvement of photocatalytic performance for CO_2 conversion, while detailed analysis on the reaction pathway and mechanism is ignored [46]. Naturally inferred, it's difficult for CO_2 to directly accept photo-induced electrons to get reduced since this process in water requires excited high-level-energy electrons below –1.9 V thermodynamically [47]. Thus, it's more possible for CO_2 to react with the produced H atoms by oxidation between photo-induced electrons and H_2O to gradually transform into CH_4 and CO [48]. However, the above inference still lacks convincing evidences. Therefore, it's rather meaningful to clarify the related process mechanism.

Based on the above considerations, we have successfully designed and fabricated the Al–O bridged $\text{g-C}_3\text{N}_4/\alpha\text{-Fe}_2\text{O}_3$ Z-scheme nanocomposites as efficient photocatalysts for CO_2 conversion and phenol degradation. The promoted charge separation and transfer by constructing the $\text{g-C}_3\text{N}_4/\alpha\text{-Fe}_2\text{O}_3$ heterojunctions as well as Al–O bridges has been evidenced by atmosphere-controlled transient-state surface photovoltage technique and measurement of produced $\cdot\text{OH}$ amounts [49,50]. Comparing with P–O and Si–O bridges, Al–O ones indicate the strongest electron shuttling ability. Besides, the Z-scheme electron transfer mechanism has been verified by the single-wavelength photocurrent action spectra and single-wavelength photoactivities for CO_2 conversion. Moreover, it is suggested by means of electrochemical and isotope experiments that the produced H atoms as the active radicals would be much favorable to induce the reduction of CO_2 to CO and CH_4 . Certainly, this work will help to understand the charge transfer and separation processes in the fabricated Z-scheme heterojunctions with deeper recognition, and provide reasonable design strategy for the $\alpha\text{-Fe}_2\text{O}_3$ -based photocatalysts applied in energy production and environmental remediation.

2. Experimental

All the chemicals in this study were of analytical grade and used as received without further purification. Deionized water was used throughout the experiments.

2.1. Materials synthesis

Nanocrystalline $\alpha\text{-Fe}_2\text{O}_3$ was synthesized by a phase-separated hydrolysis-solvothermal method. *n*-Butyl alcohol as the organic solvent and hydrated ferric nitrate $\text{Fe}(\text{NO}_3)_3 \cdot 9\text{H}_2\text{O}$ as the iron source were used. In a typical procedure, 10 mL of 5 wt.% ammonia solution was added into a 50 mL Teflon-lined autoclave and a 10 mL weighing bottle containing a solution of 0.8 g $\text{Fe}(\text{NO}_3)_3 \cdot 9\text{H}_2\text{O}$ in 8 mL *n*-butyl alcohol was placed in the autoclave with a support between the autoclave bottom and the weighing bottle. The Teflon-lined autoclave was kept at 140 °C for 6 h. After being cooled to the room temperature, the sample was washed for several times with ethanol and deionized water in turn and then dried in an oven at 80 °C to obtain nanocrystalline $\alpha\text{-Fe}_2\text{O}_3$. The bare $\alpha\text{-Fe}_2\text{O}_3$ is represented by F.

$\text{g-C}_3\text{N}_4$ was synthesized by heating urea in an alumina combustion boat at 550 °C for 4 h with a heating rate of 0.5 °C/min. After that, the furnace was cooled to the room temperature naturally. The obtained light-yellow product was grinded into fine powders for further experimental work.

To fabricate $\text{g-C}_3\text{N}_4/\alpha\text{-Fe}_2\text{O}_3$, different amounts of $\text{g-C}_3\text{N}_4$ were

mixed with 1 g α -Fe₂O₃ in a beaker and dispersed in 20 mL of 50% ethanol solution under vigorously stirring for 4 h, followed by ultrasonication for 1 h. Subsequently, the reaction mixture was kept on a hot plate and heated at 80 °C under vigorous stirring to evaporate the solvent. After being dried in an oven at 80 °C, the mixture was calcined at 400 °C for 1 h in a muffle furnace with a heating rate of 5 °C/min. The obtained nanocomposite was represented by XCN-F, where CN stands for g-C₃N₄, F means α -Fe₂O₃, and X is the mass percent of g-C₃N₄ in the composite.

The Al–O bridged g-C₃N₄/α-Fe₂O₃ was prepared by a two-step wet chemical method with AlCl₃ aqueous solution as the Al–O source. Firstly, a certain amount of as-prepared α -Fe₂O₃ nanoparticles and 0.11 g AlCl₃ were put into an ethanol/water system (50% ethanol solution) to form a mixture. The mixture was kept under stirring at 60 °C until the solvent was evaporated. After being dried in an oven, the mixture was calcined at 400 °C for 1 h. Thus, Al-modified α -Fe₂O₃ was obtained. Furthermore, 0.85 g Al-modified α -Fe₂O₃ was mixed with 0.15 g-C₃N₄, and then dispersed in 20 mL of 50% ethanol solution under stirring for 4 h, followed by ultrasonication for 1 h. Subsequently, the mixture was dried at 80 °C and then calcined at 400 °C for 1 h. As a result, Al–O-bridged g-C₃N₄/α-Fe₂O₃ was obtained and denoted by 15CN-YAl-F, in which Al means Al–O bridges, 15 is the mass percent of g-C₃N₄ in the composite and Y is the mole percent of Al to Fe.

2.2. Characterization techniques

The X-ray powder diffraction (XRD) patterns of the samples were measured with a Bruker D8 advance diffractometer, using CuK α radiation. The UV-vis diffuse reflectance spectra (UV-vis DRS) of the samples were measured with a Model Shimadzu UV2550 spectrophotometer, using BaSO₄ as a reference. The compositions and elemental chemical states of the samples were confirmed through X-ray photoelectron spectroscopy (XPS) using a Kratos-Axis Ultra DLD apparatus with an Al (mono) X-ray source. Transmission electron microscopy (TEM) and high resolution TEM (HRTEM) images of the samples were taken by a JEOL JEM-2010 electron microscope with a high acceleration voltage of 200 kV.

The steady-state surface photovoltage spectroscopy (SS-SPS) measurements of the samples were carried out with a home-built apparatus, equipped with a lock-in amplifier (SR830) synchronized with a light chopper (SR540) at different atmospheres. The powder sample was sandwiched between two indium-tin-oxide (ITO) glass electrodes kept in an atmosphere-controlled sealed container. A monochromatic light was obtained from 500 W Xenon lamp (CHF XQ500W, Global Xenon lamp power) through a double prism monochromator (SBP300). The transient-state surface photovoltage (TS-SPV) measurements were performed with a self-assembled device in air at room temperature, in which the sample chamber was connected to an ITO glass as the top electrode and a steel substrate as the bottom electrode, and about 10 mm thick mica spacer was placed between the ITO glass and the sample to decrease the space charge region at the interface between ITO and the sample. The samples were excited by a 355 nm laser radiation with 10 ns pulse width from a second harmonic Nd:YAG laser (Lab-130-10H, Newport, Co.). The laser intensity was modulated with an optical neutral filter and measured by a high energy pyroelectric sensor (PE50BF-DIFC, Ophir Photonics Group). The signals were registered by a 1 GHz digital phosphor oscilloscope (DPO 4104B, Tektronix) with an amplifier at the aid of a computer.

2.3. Photoelectrochemical measurements

Photoelectrochemical (PEC) experiments were performed in a glass cell with 1 M NaOH solution as the electrolyte using the as-prepared film as the working electrode, Pt wire (99.9%) as the counter electrode, and a saturated KCl Ag/AgCl electrode as the reference electrode. High purity nitrogen gas (99.999%) was bubbled through the electrolyte

before and during the experiments. Applied potentials were controlled by a commercial computer-controlled potentiostat (AUTOLAB PG STAT 101). The photocurrent densities at different excitation wavelengths were measured, in which monochromatic light was obtained by passing light from a 500 W Xenon lamp through a monochromator (CM110, Spectral Products). Electrochemical impedance spectra (EIS) were performed using a three-electrode configuration with the Princeton Applied Research Versa STAT 3 and carried out over the frequency range from 10² to 10⁵ Hz with an amplitude of 10 mV (Root Mean Square) at the applied bias of 0.4 V in a 1.0 M NaOH solution, using a 300W Xenon light as the illumination source.

2.4. Evaluation of produced ·OH amount

To measure the ·OH amount, 0.02 g powder sample was dispersed in 50 mL of 1×10^{-3} mol/L coumarin aqueous solution in a quartz reactor and kept under dark for 10 min to reach adsorption-desorption equilibrium. Each sample was irradiated for 1 h under 150W Xenon lamp. After centrifugation, a certain amount of the solution was taken in a Pyrex glass cell for fluorescence measurement of 7-hydroxycoumarin at 390 nm excitation wavelength and 460 nm emission wavelength through a spectrofluorometer (Perkin-Elmer LS55).

2.5. Evaluation of photoactivities

2.5.1. Photocatalytic activities for CO₂ conversion

0.2 g powder sample was dispersed in 5 mL water (pH = 7) in a cylindrical steel reactor with 100 mL volume and 3.5 cm² area. A 300 W Xenon arc lamp was used as the light source. Highly pure CO₂ gas was passed through water and then entered into the reaction setup for reaching ambient pressure. The used photocatalyst was allowed to equilibrate in the CO₂/H₂O system for 1 h. During irradiation, about 1 mL of gas produced was taken from the reaction cell at given time intervals for CO and O₂ concentration analysis using a gas chromatograph (GC-7920 with Thermal Conductivity Detector (TCD), Au Light, Beijing), and for CH₄ concentration analysis using a gas chromatograph (GC-2014 with Flame Ionization Detector (FID), Shimadzu Co., Japan).

A 100 W single-wavelength LED lamp was used as the light source to measure the single-wavelength activities for CO₂ conversion and the products were analyzed by using a gas chromatograph (GC-7920 with TCD, Au Light, Beijing). The isotopic experiments for CO₂ reduction by using D₂O and ¹³CO₂ were performed with a gas chromatograph-mass spectrometer (GC/MASS, GC-7890B/MS5977A, America Aligent).

2.5.2. Photocatalytic activities for H₂ evolution

To test hydrogen evolution, the experiments were carried out in an online cylindrical quartz cell (250 mL volume and 7.5 cm² area) connected to a closed gas circulation system, and the gases evolved were analyzed with an online TCD gas chromatograph (GC-7900, Techcomp, China). In a typical photocatalytic reaction, 0.1 g powder sample was dispersed in 100 mL H₂O. The suspension was thoroughly irradiated by a 300 W Xenon lamp. The gas evolved was measured at 1 h interval under light irradiation.

2.5.3. Photocatalytic activities for phenol degradation

The photocatalytic activities of the samples were further evaluated by the degradation of phenol. For phenol degradation, 0.2 g powdered photocatalyst and 50 mL of 10 mg/L phenol solution were mixed in a photochemical glass reactor under magnetic stirring at room temperature and standard pressure. Prior to irradiation, the mixture was stirred magnetically in dark for 30 min to reach adsorption-desorption equilibrium. After irradiation for certain time, the solution was centrifuged and then its phenol concentration was measured with a Shimadzu UV-2550 spectrophotometer through the 4-aminoantipyrine spectrophotometric method at the characteristic optical absorption.

2.6. Measurement for CO₂ temperature-programmed desorption

Temperature-programmed desorption (TPD) of CO₂ was performed in a conventional apparatus by Chemisorption Analyzer (Tp 5080 Chemisorb) equipped with a TCD. About 50 mg samples were preheated to 300 °C for 1 h to remove the moisture, and then cooled down to room temperature under an ultra-high-pure He gas with the flow rate of 30 mL/min. Highly pure CO₂ gas was introduced at a constant temperature of 30 °C under the flow rate of 30 mL/min for 60 min. The physically adsorbed CO₂ was removed by being exposed with ultra-high-pure He at 30 °C for 60 min. Then the temperature was increased to 700 °C with the heating rate of 10 °C/min under ultra-high-pure He. The desorbed CO₂ was analyzed by Chemisorption Analyzer (Tp 5080 Chemisorb).

2.7. Electrochemical reduction measurement

Electrochemical reduction experiments were performed in a conventional three-electrode system, using a saturated calomel electrode (SCE) and a Pt plate as the reference electrode and the counter electrode, respectively. A 0.3 cm diameter glassy carbon (GC) electrode was used as the working electrode. 5 mg catalyst mixed with 20 μL of 5 wt. % Nafion ionomers were dispersed in 0.18 mL alcohol solution (50 wt. % ethanol solution). After the catalyst ink was sonicated for 0.5 h, an appropriate volume of the ink was evenly dropped onto the well-polished GC electrode surface and dried at ambient temperature. Electrochemical activity and stability of catalysts were tested with a BAS 100 B electrochemical workstation. Initially, electrode potentials were cycled between two potentials to keep perfectly overlapping, and then subsequent voltammograms were obtained. The electrolyte for test was 1 M NaOH. All the tests were carried out at the room temperature.

3. Results and discussion

3.1. Structural characterization

In Fig. S1, the XRD diffraction peaks at around 24.1°, 33.2°, 35.6°, 42.1°, 49.4° and 54.1° are attributed to α-Fe₂O₃ according to the standard card JCPDS 33-0664, respectively corresponding to the (012), (104), (110), (113), (024) and (116) crystal planes [51]. Pure g-C₃N₄ shows a characteristic diffraction peak at around 27.3°, which can be assigned to the interlayer stacking aromatic systems, indexed to (002) facet of graphitic materials [52]. As for the fabricated g-C₃N₄/α-Fe₂O₃ nanocomposites and Al–O bridged ones, there exist two phases as ascribed to g-C₃N₄ and α-Fe₂O₃, respectively. Noticeably, the diffraction peaks of α-Fe₂O₃ show no obvious changes, indicating that its crystallinity has been well maintained in the fabricated nanocomposites.

The UV-vis DRS spectra (Fig. S2) indicate that the optical absorption behavior of α-Fe₂O₃ has not been affected after coupling g-C₃N₄ or further constructing Al–O bridges. It is evaluated that its optical absorption threshold of α-Fe₂O₃ is about 630 nm, corresponding to 1.97 eV by the widely-accepted energy bandgap equation ($\lambda = 1240/E_g$). Based on the TEM image (Fig. 1A), it is seen that the Al–O bridged g-C₃N₄/α-Fe₂O₃ nanocomposite has an average diameter of ca. 20 nm, and α-Fe₂O₃ nanoparticles are connected with g-C₃N₄ nanosheets successfully. Additionally, in the area-selected HRTEM image (Fig. 1B) α-Fe₂O₃ and g-C₃N₄ have shown an intimate contact. The lattice fringes at the inter-planar distance of 0.25 nm are attributed to α-Fe₂O₃. Based on above, the heterojunction between α-Fe₂O₃ and g-C₃N₄ has been successfully formed. Certainly, the intimate connection is vital for the effective charge transfer in the heterojunctional nanocomposites.

In order to confirm the elemental chemical states, XPS spectra were measured, as shown in Fig. S3. As illustrated in Fig. S3A, one can see that the Fe2p spectra of unbridged and Al–O bridged g-C₃N₄/α-Fe₂O₃ are similar. Two distinct peaks at 710.7 eV with a shake-up satellite at 718.20 eV and 724.1 eV with a shake-up satellite at 732.9 eV are

ascribed to Fe2p_{3/2} and Fe2p_{1/2}, respectively, and it is characteristic of Fe³⁺ in α-Fe₂O₃. The O1s spectra of both samples are fitted into two contributions according to the Gaussian rule with origin software. These contributions located at 529.5 eV and 531.6 eV (Fig. S3B) are attributed to crystal lattice oxygen and hydroxyl oxygen, respectively [53]. The intensity of the hydroxyl oxygen peak at 531.6 eV obviously increases after building the Al–O bridges. A clear peak of N1s on 15CN-F is centered at 399.0 eV, assigned to sp² hybridized nitrogen (C=N=C). Two peaks of C1s at 284.5 eV and 288.6 eV are ascribed to the contaminated carbon and the sp²C atoms – bonded to N in the aromatic cycle (N=C=N)=, respectively. It is noticed from Fig. S3C and D, that the binding energies of N1s and C1s (C=N) are shifted towards the low energy side after creating Al–O bridges, demonstrating the electron delocalization effect of created Al–O bridges. As expected, the XPS spectrum of 15CN-6Al-F shows an obvious Al2p peak at 73.8 eV (Fig. S3E) [54]. In general, it is acceptable that the –Al–OH groups could connect with g-C₃N₄ and α-Fe₂O₃ through the surface adsorbed hydroxyls by the dehydration process at the aid of thermal treatment. Thus, it is deduced that the Al–O bridges are successfully incorporated into the g-C₃N₄/α-Fe₂O₃ nanocomposites, which would act as effective bridges for charge transfer.

3.2. Photophysical and photochemical properties

The photo-induced electron-hole formation and separation of solid semiconductor materials can be analyzed through a highly sensitive SS-SPS technique. For a nanosized semiconductor, its SS-SPS response derives from the photo-induced charge separation via the diffusion process since its built-in electric field is usually neglected. In general, the strong SS-SPS response frequently corresponds to the high photo-induced charge separation. It is clear that α-Fe₂O₃ shows a low SS-SPS response (Fig. 2A and Fig. S4). However, its SS-SPS signal is obviously enhanced after coupling with an appropriate amount of g-C₃N₄, especially for 15CN-F nanocomposite. Interestingly, it is found that the SS-SPS response of 15CN-F significantly increases by constructing Al–O bridges between α-Fe₂O₃ and g-C₃N₄. Obviously, the strongest SS-SPS response is observed for the 15CN-6Al-F. Thus, it is confirmed that the photo-induced charge separation of α-Fe₂O₃ could be enhanced by constructing heterojunction with g-C₃N₄ and further enhanced by creating Al–O bridges. However, if the used amounts of g-C₃N₄ and Al–O bridges are excessive, the SS-SPS responses would decrease.

Meanwhile, the TS-SPV technique was applied to investigate the dynamic processes of photo-induced charge carriers. During the TS-SPV measurements, the samples were excited by a 355 nm-laser radiation with 10 ns pulse. According to the principle of TS-TPV, the charge separation of nanosized semiconductor is mainly influenced by the carrier diffusion process, leading to an obviously slow TS-SPV response ($> 10^{-4}$ s). Since the photo-induced electrons of α-Fe₂O₃ are captured by adsorbed O₂, it is understandable that the diffusion of positive holes to the surface is much faster than that of captured negative electrons, leading to a positive TS-SPV response (Fig. 2B). Similarly, the highest TS-SPV response is observed for 15CN-6Al-F, indicating the highest photo-induced charge separation. Noticeably, the carrier lifetime of α-Fe₂O₃ is prolonged by ~ ms after forming heterojunction with g-C₃N₄, especially for the built Al–O bridged ones. Hence, the long-lived photo-induced charge carriers mean the high photo-induced charge separation. This is in good agreement with the above-mentioned SS-SPS results on the greatly-enhanced charge separation.

In order to further confirm the enhanced charge separation, we have also carried out the PEC experiments, as shown in (Fig. 2C) and (Fig. S5). The large photocurrent density usually corresponds to the high photo-induced charge separation. It is noticed that the photocurrent density of α-Fe₂O₃ is greatly enhanced after coupling g-C₃N₄, and it is clear that the highest photocurrent response is observed for 15CN-F. As expected, the photocurrent density of 15CN-F is further enhanced after creating Al–O bridges. In particular, a significant enhancement is

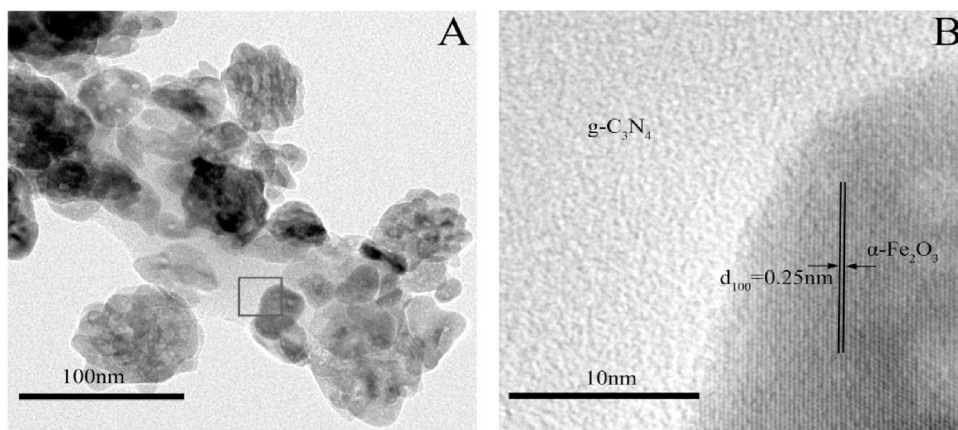


Fig. 1. TEM image of 15CN-6Al-F (A) with an area-selected HRTEM (B). (F, CN and Al mean $\alpha\text{-Fe}_2\text{O}_3$, $\text{g-C}_3\text{N}_4$ and Al–O bridges, respectively. X in XCN is the mass percent of $\text{g-C}_3\text{N}_4$ used in the composite, and Y in YAl is the mole percent of Al relative to Fe. It is the same unless stated elsewhere.).

observed for 15CN-6Al-F. This indicates that the resulting 15CN-6Al-F exhibits a high photo-induced charge separation. However, the photocurrent density decreases with over amount of $\text{g-C}_3\text{N}_4$ and Al–O bridges. In addition, the coumarin fluorescent method was employed to detect the amount of formed $\cdot\text{OH}$, in which the coumarin easily reacts with $\cdot\text{OH}$ and then to produce luminescent 7-hydroxycoumarin. In general, the stronger fluorescent signal corresponds to the higher produced $\cdot\text{OH}$. As shown in Fig. 2D and Fig. S6, $\alpha\text{-Fe}_2\text{O}_3$ shows a small amount of $\cdot\text{OH}$. After coupling with a proper amount of $\text{g-C}_3\text{N}_4$, the amount of produced $\cdot\text{OH}$ obviously increases, especially with 15CN-F. Interestingly, the amount of produced $\cdot\text{OH}$ for 15CN-F further increases after introducing Al–O bridges to 15CN-F, and it exhibits the largest amount of $\cdot\text{OH}$ on 15CN-6Al-F. Obviously, this is well consistent with the above SS-SPS, TS-SPV and photocurrent results. Therefore, based on the photophysical and photochemical results, it is clearly demonstrated that the photo-induced charge separation of $\alpha\text{-Fe}_2\text{O}_3$ could be enhanced by fabricating nanocomposites with $\text{g-C}_3\text{N}_4$ with proper amounts, especially for the created Al–O bridged ones. Further, it is anticipated that the Al–O bridged $\text{g-C}_3\text{N}_4/\alpha\text{-Fe}_2\text{O}_3$ nanocomposites would display high photocatalytic activities compared to bare $\alpha\text{-Fe}_2\text{O}_3$ and $\text{g-C}_3\text{N}_4/\alpha\text{-Fe}_2\text{O}_3$ nanocomposites.

Fe₂O₃ nanocomposites.

3.3. Photocatalytic activities for CO₂ conversion and phenol degradation

The photocatalytic activities of as-prepared samples were evaluated for CO₂ reduction and phenol degradation, as shown in Fig. 3, and Fig. S7 and S8. It is confirmed that the detected gas products of CO₂ reduction contain CO and CH₄, especially for CO, simultaneously with a certain amount of O₂ produced as a result of H₂O oxidation. It is seen from Fig. 3A that $\alpha\text{-Fe}_2\text{O}_3$ exhibits a weak photocatalytic activity for the reduction of CO₂ to produce CO ($\sim 5.7 \mu\text{mol g}^{-1} \text{ h}^{-1}$), CH₄ ($\sim 0.3 \mu\text{mol g}^{-1} \text{ h}^{-1}$) and O₂ ($\sim 6.2 \mu\text{mol g}^{-1} \text{ h}^{-1}$) after irradiating for 1 h. Noticeably, its photoactivity is improved after introducing a certain amount of $\text{g-C}_3\text{N}_4$, and it is much obvious for 15CN-F samples to produce CO ($\sim 15.8 \mu\text{mol g}^{-1} \text{ h}^{-1}$), CH₄ ($\sim 3.1 \mu\text{mol g}^{-1} \text{ h}^{-1}$) and O₂ ($\sim 18.5 \mu\text{mol g}^{-1} \text{ h}^{-1}$). However, the activity begins to decrease when the amount of used CN is in excess, like 20CN-F. Interestingly, the photocatalytic activity of the resulting 15CN-F nanocomposite could be further improved by constructing Al–O bridges between $\text{g-C}_3\text{N}_4$ and $\alpha\text{-Fe}_2\text{O}_3$, and 15CN-6Al-F is the amount-optimized one to produce CO

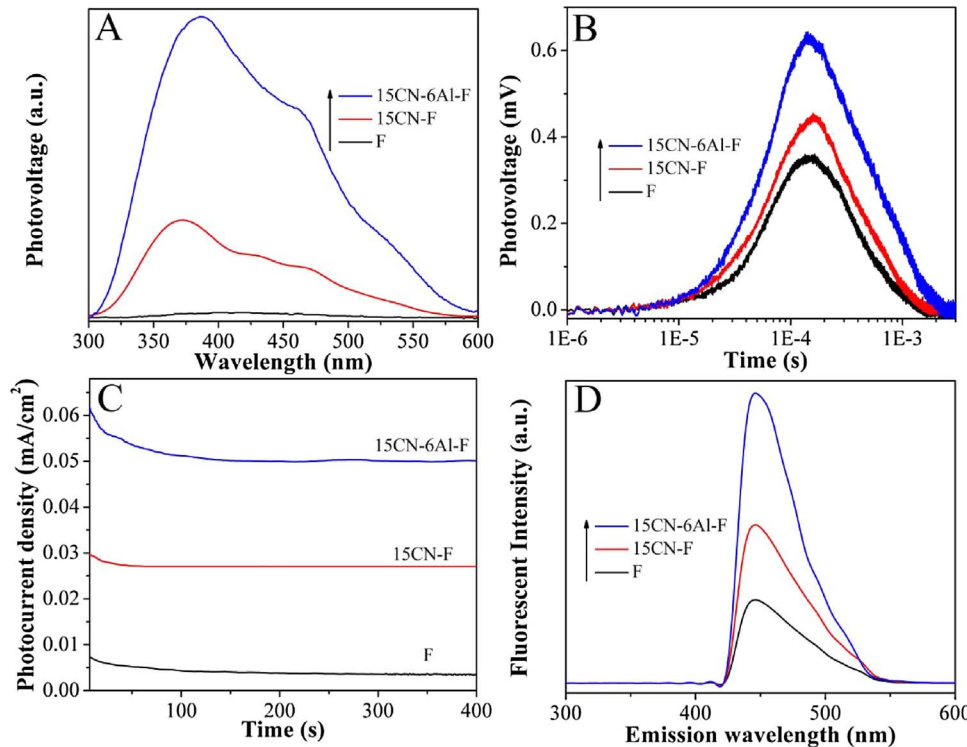
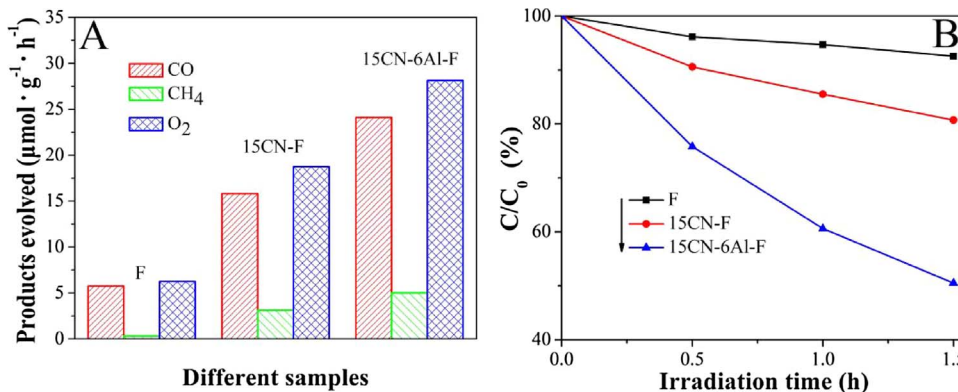


Fig. 2. SS-SPS responses in air (A), TS-SPV responses in air (B), PEC I-t curves (C) and fluorescence spectra related to the formed $\cdot\text{OH}$ amounts after irradiation for 1 h (D) of F, 15CN-F and 15CN-6Al-F.



(~ 24 μmol·g⁻¹·h⁻¹), by ~ 4-time enhancement relative to that of α-Fe₂O₃.

The improved photocatalytic activities of fabricated samples were further supported by the degradation of phenol under irritation for 1 h (Fig. 3B). It is clear that the photocatalytic activity of bare α-Fe₂O₃ for phenol degradation is relatively low. However, an obvious enhancement is observed when g-C₃N₄ is coupled onto α-Fe₂O₃ with a proper amount, and 15CN-F shows the highest photocatalytic activity. As expected, further improvement in the photocatalytic activity is seen for phenol degradation when Al–O bridges are introduced between g-C₃N₄ and α-Fe₂O₃. In particular, 15CN-6Al-F displays the best photocatalytic degradation performance. Thus, it is clearly demonstrated that the photocatalytic activities of α-Fe₂O₃ for CO₂ conversion and phenol degradation could be greatly improved by coupling an Al–O bridged g-C₃N₄, attributed to markedly enhanced photo-induced charge separation. The stability of 15CN-6Al-F sample was tested by consecutive reactions, as shown in Fig. S9. It is noticed that the photoactivity for producing CO nearly keeps unchanged during 5 cycles, indicating that it is robust during the photocatalytic processes and hence promising for the practical applications.

3.4. Discussion on mechanism

As described above, the photo-induced charge separation of α-Fe₂O₃ could be markedly promoted by constructing g-C₃N₄/α-Fe₂O₃ nanocomposites. According to the band energy structures of g-C₃N₄ and α-Fe₂O₃, the charge transfer and separation is commonly considered to obey the Z-scheme mechanism. In order to confirm the Z-scheme mechanism, we have recorded single-wavelength photocurrent action spectra, as shown in Fig. 4A. It is well accepted that the optical absorption thresholds of α-Fe₂O₃ and g-C₃N₄ are 630 and 460 nm, respectively. One can see that the photocurrent density of α-Fe₂O₃ evenly increases as the excitation wavelength decreases from 600 nm to 400 nm. For 15CN-F nanocomposite, it is similar to α-Fe₂O₃ when the

excitation wavelength is not shorter than 500 nm. In this case, g-C₃N₄ could not be excited. When the used excitation wavelength is 450 nm, the observed photocurrent density of 15CN-F sharply increases. Naturally accepted, α-Fe₂O₃ and g-C₃N₄ are excited simultaneously to produce electron-hole pairs. Therefore, the sharp increase in the photocurrent density is attributed to the Z-scheme mechanism on the photo-induced charge transfer and separation. Noticeably, its photocurrent density still continues to become large as the excitation wavelength is further decreased. The Al–O bridged 15CN-F (15CN-6Al-F) exhibits a much large photocurrent density compared to the unbridged 15CN-F with the excitation wavelength below 450 nm. This indicates the created Al–O bridges between α-Fe₂O₃ and g-C₃N₄ facilitate the photo-induced charge transfer and separation.

EIS Nyquist plots (Fig. S10) further confirm the promoted charge transfer in the g-C₃N₄/α-Fe₂O₃ nanocomposites. It is seen that the capacitive arc radius of α-Fe₂O₃ is decreased after integration with g-C₃N₄, especially for the Al–O bridged one. The decreased capacitive arc radii correspond to the enhanced charge transfer and separation. To further verify the Z-scheme mechanism, we also measured the single-wavelength activities for CO₂ conversion on 15CN-6Al-F, as shown in Fig. 4B. It is noticed that the amount of produced CO gradually increases as the excitation wavelength is decreased to 470 nm, while an obviously increased photocurrent is observed at 450 nm. This is in good agreement with the above observed photocurrent densities. In addition, it is confirmed as Fig. S11 that the P–O and Si–O bridges built by similar procedures are also favorable for the photo-induced charge transfer and separation on the fabricated g-C₃N₄/α-Fe₂O₃ nanocomposites on the conditions of the same amounts used, leading to the improved photoactivities. It is worthy of noting that the created Al–O bridges are the best among the built three ones.

To investigate the mechanism of photocatalytic reduction of CO₂, the electrochemical reduction curves were carried out in different gas-bubbled systems, as shown in Fig. 5. In the N₂-bubbled system, it is noticed that it is much favorable for H₂ evolution on the fabricated g-

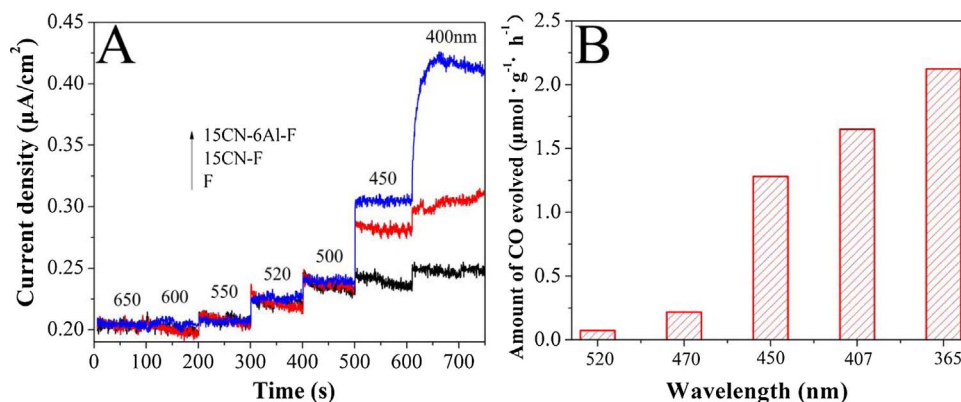


Fig. 4. Single-wavelength photocurrent action spectra of F, 15CN-F and 15CN-6Al-F (A) and single-wavelength photoactivities for CO₂ conversion of 15CN-6Al-F (B).

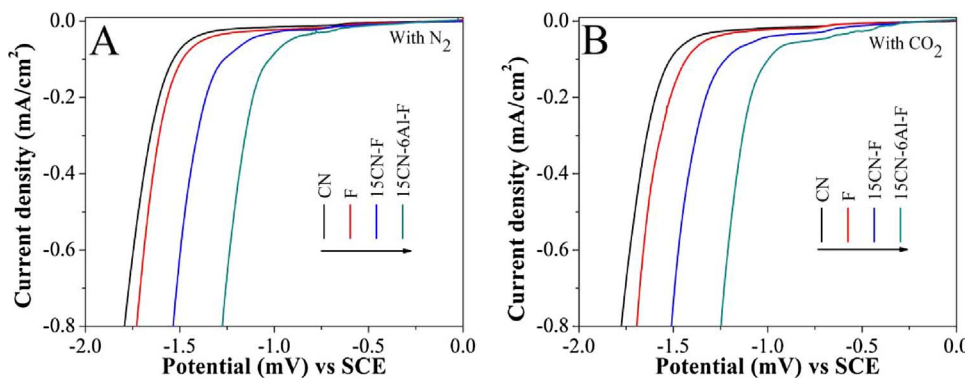


Fig. 5. Electrochemical reduction curves in the N_2 -bubbled (A) and CO_2 -bubbled (B) systems of CN, F, 15CN-F and 15CN-6Al-F. (PEC measurements were performed with a three-electrode system in 1 M NaOH electrolyte, with the tested film as the working electrode, Ag/AgCl as the reference electrode, and Pt plate as the counter electrode).

$\text{C}_3\text{N}_4/\alpha\text{-Fe}_2\text{O}_3$ nanocomposite (15CN-F) based on the onset potential, especially for the Al–O bridged one (15CN-6Al-F). This indicates that it is favored thermodynamically to evolve H_2 on 15CN-6Al-F. In addition, it's worthy of noting that the onset potentials of different Fe_2O_3 -based electrodes for H_2 evolution are similar to those in the CO_2 -bubbled system. This clearly indicates that the observed current response mainly results from the H_2O reduction, other than from the CO_2 reduction. This is because that it's not beneficial to enhance the capacity of $\alpha\text{-Fe}_2\text{O}_3$ to adsorb CO_2 by integrating with $\text{g-C}_3\text{N}_4$ according to the recorded temperature-programmed desorption curves of CO_2 (Fig. S12). Moreover, it is confirmed that a certain amount of H_2 could be produced during the photocatalytic process only in water on 15CN-6Al-F (Fig. S13). Thus, it is suggested that the produced H atoms play key roles to initiate the photocatalytic reduction of CO_2 .

In addition, it is confirmed by Fig. S14 that it is also much favorable for O_2 reduction on the fabricated $\text{g-C}_3\text{N}_4/\alpha\text{-Fe}_2\text{O}_3$ nanocomposite (15CN-F), especially for the Al–O bridged one (15CN-6Al-F). This demonstrates that thermodynamically adsorbed O_2 is inclined to capture photo-induced electrons, leading to the promoted charge separation and hence to the enhanced photocatalytic activity for degrading phenol. To further verify if the H atoms originate from the photocatalytic reduction of H_2O and then anticipate in the conversion of CO_2 , we have carried out isotopic experiments by using $^{13}\text{CO}_2$ and D_2O under the identical photocatalytic reaction conditions. The resultant photocatalytic products have been identified and quantified with GC–MS. As shown in Fig. S15A, ^{13}C , ^{13}CH , $^{13}\text{CH}_2$, $^{13}\text{CH}_3$ and $^{13}\text{CH}_4$ have been detected. This indicates that the produced CH_4 indeed derives from the reduction of CO_2 . When H_2O is replaced by D_2O , as shown in Fig. S15 B, C, CD, CD_2 , CD_3 , and CD_4 have been detected, indicating that the H atoms in produced CH_4 originate from H_2O . This further supports that the produced H atoms dominantly induce the photocatalytic CO_2 conversion.

Based on the above results and discussion, a schematic on the transfer and separation of photo-induced charges for the fabricated Al–O bridged $\text{g-C}_3\text{N}_4/\alpha\text{-Fe}_2\text{O}_3$ nanocomposites and the induced photochemical processes have been proposed, as shown in Fig. 6. When both $\alpha\text{-Fe}_2\text{O}_3$ and $\text{g-C}_3\text{N}_4$ are excited simultaneously below 460 nm, the photo-induced electrons of $\alpha\text{-Fe}_2\text{O}_3$ would combine with the photo-induced holes of $\text{g-C}_3\text{N}_4$ in the fabricated $\text{g-C}_3\text{N}_4/\alpha\text{-Fe}_2\text{O}_3$ nanocomposites. In this case, the spatially separated holes on $\alpha\text{-Fe}_2\text{O}_3$ and electrons on $\text{g-C}_3\text{N}_4$ would possess sufficient energy to thermodynamically induce redox reactions, leading to the promoted charge separation and hence the improved photocatalytic activities.

In particular, the introduction of Al–O bridges into the nanocomposites is much favorable for the charge separation by promoting the charge transfer from $\alpha\text{-Fe}_2\text{O}_3$ to $\text{g-C}_3\text{N}_4$, consequently further improving the photoactivities for CO_2 conversion and phenol degradation. In the degradation of phenol, the photo-induced electrons on $\text{g-C}_3\text{N}_4$ could easily be captured by the adsorbed O_2 to produce $\cdot\text{O}_2^-$, while the photo-induced holes of $\alpha\text{-Fe}_2\text{O}_3$ could initiate the oxidation with H_2O to produce $\cdot\text{OH}$, further attacking phenol. In the conversion of CO_2 , the

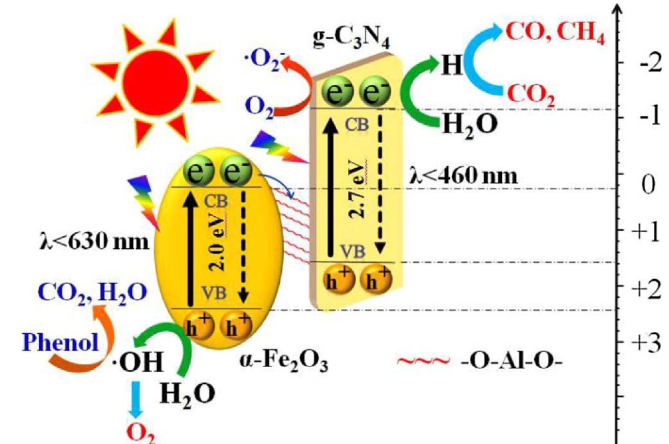


Fig. 6. Schematic on the transfer and separation of photo-induced charges in the fabricated Al–O bridged $\text{g-C}_3\text{N}_4/\alpha\text{-Fe}_2\text{O}_3$ nanocomposites and the induced photochemical reactions.

photo-induced electrons on $\text{g-C}_3\text{N}_4$ could easily induce the reduction reactions with H_2O to produce H atoms that attack CO_2 to produce CO and CH_4 , while the produced $\cdot\text{OH}$ by the reactions of photo-induced holes of $\alpha\text{-Fe}_2\text{O}_3$ with H_2O could further evolve O_2 .

4. Conclusions

In summary, we have successfully improved the photocatalytic activities of $\alpha\text{-Fe}_2\text{O}_3$ for CO_2 conversion and phenol degradation by fabricating heterojunctional nanocomposites with Al–O bridged $\text{g-C}_3\text{N}_4$. Interestingly, the created Al–O bridges in the fabricated nanocomposites further improve the photocatalytic activities. It is confirmed that the photo-induced charge separation of resulting $\text{g-C}_3\text{N}_4/\alpha\text{-Fe}_2\text{O}_3$ nanocomposites obeys a Z-scheme mechanism, in which the spatially separated electrons on $\text{g-C}_3\text{N}_4$ and holes on $\alpha\text{-Fe}_2\text{O}_3$ would possess enough energy to induce redox reactions, leading to the enhanced charge separation and hence to the improved photocatalytic activities. Moreover, it is much favorable for the charge transfer and separation to create Al–O bridges in the fabricated nanocomposites, responsible for the obviously-improved photocatalytic activities. Furthermore, it is suggested that the produced H atoms play important roles in the photocatalytic conversion of CO_2 on the fabricated nanocomposites. This work will help to understand the charge transfer and separation mechanisms in the Z-scheme heterojunctions in detail, and provide us with a much feasible route to synthesize efficient nanosized $\alpha\text{-Fe}_2\text{O}_3$ -based photocatalysts for efficient solar energy utilization to produce energy and purify environment.

Acknowledgements

We are grateful for financial support from NSFC (U1401245, 21501052, 91622119), the Program for Innovative Research Team in Chinese Universities (IRT1237), the Research Project of Chinese Ministry of Education (213011A), and the Science Foundation for Excellent Youth of Harbin City of China (2014RFYXJ002, 2016RQQXJ099).

Appendix A. Supplementary data

Supplementary data associated with this article can be found, in the online version, at <http://dx.doi.org/10.1016/j.apcatb.2017.09.042>.

References

- [1] N.J. Abram, H.V. McGregor, J.E. Tierney, M.N. Evans, N.P. McKay, D.S. Kaufman, *Nature* 536 (2016) 411–418.
- [2] R. Johan, S. Will, N. Kevin, P. Åsa, C.F. Stuart, F.L. Eric, M.L. Timothy, S. Marten, F. Carl, J.S. Hans, N. Björn, A.W. Cynthia, H. Terry, V.L. Sander, R. Henning, S. Sverker, K.S. Peter, C. Robert, S. Uno, F. Malin, K. Louise, W.C. Robert, J.F. Victoria, H. James, W. Brian, L. Diana, R. Katherine, C. Paul, A.F. Jonathan, *Nature* 461 (2009) 472–475.
- [3] J.F. Reynolds, D.M. Smith, E.F. Lambin, B.L. Turner II, M. Mortimore, S.P. Batterbury, T.E. Downing, H. Dowlatabadi, R.J. Fernández, J.E. Herrick, E. Huber-Sannwald, H. Jiang, R. Leemans, T. Lynam, F.T. Maestre, M. Ayarza, B. Walker, *Science* 316 (2007) 847–851.
- [4] A. Genua-Olmedo, C. Alcaraz, N. Caiola, C. Ibáñez, *Sci. Total. Environ.* 571 (2016) 1200–1210.
- [5] J.A. Pounds, M.R. Bustamante, L.A. Coloma, J.A. Consuegra, M.P. Fogden, P.N. Foster, E.L. Marca, K.L. Masters, A. Merino-Viteri, R. Puschendorf, S.R. Ron, G.A. Still, C.J. Sanchez-Azofeifa, B.E. Young, *Nature* 439 (2006) 161–167.
- [6] G.A. Olah, G.K. Prakash, A. Goeppert, *J. Am. Chem. Soc.* 133 (2011) 12881–12898.
- [7] W.J. Ong, L.L. Tan, S.P. Chai, S.T. Yong, A.R. Mohamed, *Nano Energy* 13 (2015) 757–770.
- [8] J. Cheng, M. Zhang, G. Wu, X. Wang, J.H. Zhou, K. Cen, *Environ. Sci. Technol.* 48 (2014) 7076–7084.
- [9] D.D. Zhou, Z.X. Xu, S.S. Dong, M.X. Huo, S.S. Dong, X.D. Tian, B. Cui, H.F. Xiong, T.T. Li, D.M. Ma, *Environ. Sci. Technol.* 49 (2015) 7776–7783.
- [10] G. Busca, S. Berardinelli, C. Resini, L. Arrighi, J. Hazard. Mater. 160 (2008) 265–288.
- [11] J. Tian, Y.H. Leng, Z.H. Zhao, Y. Xia, Y.H. Sang, P. Hao, J. Zhan, M.C. Li, H. Liu, *Nano Energy* 11 (2015) 419–427.
- [12] S.N. Habisreutinger, L. Schmidt-Mende, J.K. Stolarczyk, *Angew. Chem. Int. Edit.* 52 (2013) 7372–7408.
- [13] H. Chen, S. Chen, X. Quan, Y.B. Zhang, *Environ. Sci. Technol.* 44 (2010) 451–455.
- [14] X.Q. Liu, J. Iocozzi, Y. Wang, X. Cui, Y.H. Chen, S.Q. Zhao, Z. Li, Z.Q. Lin, *Energy Environ. Sci.* 10 (2017) 402–434.
- [15] A. Zada, M. Humayun, F. Raziq, X.L. Zhang, Y. Qu, L.L. Bai, C.L. Qin, L.Q. Jing, H.G. Fu, *Adv. Energy Mater.* 6 (2016) 1601190.
- [16] J. Ding, L. Zhang, Q.Q. Liu, W.L. Dai, G.F. Guan, *Appl. Catal. B: Environ.* 203 (2017) 335–342.
- [17] J.F. Zhang, Y.F. Hu, X.L. Jiang, S.F. Chen, S.G. Meng, X.L. Fu, J. Hazard. Mater. 280 (2014) 713–722.
- [18] Y.S. Hu, A. Kleiman-Shwarscstein, A.J. Forman, D. Hazen, J.N. Park, E.W. McFarland, *Chem. Mater.* 20 (2008) 3803–3805.
- [19] S.H. Shen, S.A. Lindley, X.Y. Chen, J.Z. Zhang, *Energy Environ. Sci.* 9 (2016) 2744–2775.
- [20] Z.M. Zhang, C.T. Gao, Y.X. Li, W.H. Han, W.B. Fu, Y.M. He, E.Q. Xie, *Nano Energy* 30 (2016) 892–899.
- [21] L.M. He, L.Q. Jing, Y.B. Luan, L. Wang, H.G. Fu, *ACS Catal.* 4 (2014) 990–998.
- [22] S. Guo, G.K. Zhang, Y.D. Guo, J.C. Yu, *Carbon* 60 (2013) 437–444.
- [23] Y.S. Hu, A. Kleiman-Shwarscstein, G.D. Stucky, E.W. McFarland, *Chem. Commun.* 40 (2009) 2652–2654.
- [24] W.Q. Fan, Q.H. Zhang, Y. Wang, *Phys. Chem. Chem. Phys.* 15 (2013) 2632–2649.
- [25] Y.Q. Cong, M.M. Chen, T. Xu, Y. Zhang, Q. Wang, *Appl. Catal. B: Environ.* 147 (2014) 733–740.
- [26] P. Luan, M.Z. Xie, D.N. Liu, X.D. Fu, L.Q. Jing, *Sci. Rep.* 4 (2014) 6180.
- [27] Y. Tachibana, L. Vayssières, J.R. Durrant, *Nat. Photon* 6 (2012) 511–518.
- [28] Y.M. He, L.H. Zhang, B.T. Teng, M.H. Fan, *Environ. Sci. Technol.* 49 (2015) 649–656.
- [29] P. Zhou, J.G. Yu, M. Jaroniec, *Adv. Mater.* 26 (2014) 4920–4935.
- [30] J.C. Wang, L. Zhang, W.X. Fang, J. Ren, Y.Y. Li, H.C. Yao, J.S. Wang, Z.J. Li, *ACS Appl. Mater. Int.* 7 (2015) 8631–8639.
- [31] J.L. Bredas, J.E. Norton, J. Cornil, V. Coropceanu, *Acc. Chem. Res.* 42 (2009) 1691–1699.
- [32] G.S. Li, Z.C. Lian, W.C. Wang, D.Q. Zhang, H.X. Li, *Nano Energy* 19 (2016) 446–454.
- [33] J. Liu, Y. Liu, N.Y. Liu, Y.Z. Han, X. Zhang, H. Huang, Y. Lifshitz, S.T. Lee, J. Zhong, Z.H. Kang, *Science* 347 (2015) 970–974.
- [34] S.Z. Hu, R.R. Jin, G. Lu, D. Liu, J.Z. Gui, *RSC Adv.* 4 (2014) 24863–24869.
- [35] B.R. Zeng, L.C. Zhang, X.Y. Wan, H.J. Song, Y. Lv, *Sens. Actuators B: Chem.* 211 (2015) 370–376.
- [36] L. Xu, J.X. Xia, H. Xu, S. Yin, K. Wang, L.Y. Huang, L.G. Wang, H.M. Li, *J. Power Sources* 245 (2014) 866–874.
- [37] F. Chen, Q. Yang, X.M. Li, G.M. Zeng, D.B. Wang, C.G. Niu, J.W. Zhao, H.X. An, T. Xie, Y.C. Deng, *Appl. Catal. B: Environ.* 200 (2017) 330–342.
- [38] W.J. Yin, L.J. Bai, Y.Z. Zhu, S.X. Zhong, L.H. Zhao, Z.Q. Li, S. Bai, *ACS Appl. Mater. Int.* 8 (2016) 23133–23142.
- [39] W.B. Li, C. Feng, S.Y. Dai, J.G. Yue, F.X. Hua, H. Hou, *Appl. Catal. B: Environ.* 168 (2015) 465–471.
- [40] X.D. Fu, M.Z. Xie, P. Luan, L.Q. Jing, *ACS Appl. Mater. Int.* 6 (2014) 18550–18557.
- [41] P. Luan, M.Z. Xie, X.D. Fu, Y. Qu, X.J. Sun, L.Q. Jing, *Phys. Chem. Chem. Phys.* 7 (2015) 5043–5050.
- [42] G.G. Zhang, Z.A. Lan, X.C. Wang, *Angew. Chem. Int. Edit.* 55 (2016) 15712–15727.
- [43] D. Imanbaew, J. Lang, M.F. Gelin, S. Kaufhold, M.G. Pfeffer, S. Rau, C. Riehn, *Angew. Chem. Int. Edit.* 56 (2017) 5471–5474.
- [44] L.K. Ge, J.W. Chen, X.L. Qiao, J. Lin, X. Cai, *Environ. Sci. Technol.* 43 (2009) 3101–3107.
- [45] V.P. Indrakanti, J.D. Kubicki, H.H. Schobert, *Energy Environ. Sci.* 2 (2009) 745–758.
- [46] O.K. Varghese, M. Paulose, T.J. LaTempa, C.A. Grimes, *Nano Lett.* 9 (2009) 731–737.
- [47] M. Börjesson, T. Moragas, D. Gallego, R. Martin, *ACS Catal.* 6 (2016) 6739–6749.
- [48] W. Lin, K.M. Stocker, G.C. Schatz, *J. Am. Chem. Soc.* 139 (2017) 4663–4666.
- [49] J. Wu, H.W. Lu, X.L. Zhang, F. Raziq, Y. Qu, L.Q. Jing, *ChemCommun* 52 (2016) 5027–5029.
- [50] L.L. Peng, T.F. Xie, Y.C. Lu, H.M. Fan, D.J. Wang, *Phys. Chem. Chem. Phys.* 12 (2010) 8033–8041.
- [51] H.W. Wang, Z.J. Xu, H. Yi, H.G. Wei, Z.H. Guo, X.F. Wang, *Nano Energy* 7 (2014) 86–96.
- [52] J.H. Wang, Y.L. Chen, Y.F. Shen, S.Q. Liu, Y.J. Zhang, *ChemCommun* 53 (2017) 2978–2981.
- [53] Y.Q. Cong, M.M. Chen, T. Xu, Y. Zhang, Q. Wang, *Appl. Catal. B: Environ.* 147 (2014) 733–740.
- [54] F.T. Li, S.J. Liu, Y.B. Xue, X.J. Wang, Y.J. Hao, J. Zhao, *Chem. Eur. J.* 21 (2015) 10149–10159.